Nonlinear frequency conversion using high-quality modes in GaAs nanobeam cavities

Sonia Buckley,[1,*] Marina Radulaski,[1] Jingyuan Linda Zhang,[1] Jan Petykiewicz,[1] Klaus Biermann,[2] and Jelena Vučković[1]

[1]*Ginzton Laboratory, Spilker Engineering and Applied Sciences Building, Stanford University, Stanford, California 94305, USA*

[2]*Paul-Drude-Institut für Festkörperelektronik, Hausvogteiplatz 5-7, D-10117 Berlin, Germany*

**Corresponding author: bucklesm@stanford.edu*

Received July 10, 2014; revised August 20, 2014; accepted August 21, 2014; posted August 22, 2014 (Doc. ID 216478); published September 25, 2014

We demonstrate the design, fabrication, and characterization of nanobeam photonic crystal cavities in (111)-GaAs with multiple high-Q modes, with large frequency separations (up to 740 nm in experiment, i.e., a factor of 1.5 and up to an octave in theory). Such structures are crucial for efficient implementation of nonlinear frequency conversion. Here, we employ them to demonstrate sum-frequency generation from 1300 and 1950 nm to 780 nm. These wavelengths are particularly interesting for quantum frequency conversion between Si vacancy centers in diamond and the fiber-optic network. © 2014 Optical Society of America

OCIS codes: (350.4238) Nanophotonics and photonic crystals; (190.4390) Nonlinear optics, integrated optics.
http://dx.doi.org/10.1364/OL.39.005673

Photonic crystal cavities show great promise for nonlinear frequency conversion, due to their high-quality (Q) factors and low mode volumes, which increase the conversion efficiency. $\chi^{(3)}$ processes such as Raman lasing [1] and third-harmonic generation [2] in high-Q silicon photonic crystal cavities as well as the $\chi^{(2)}$ processes of second-harmonic generation (SHG) and sum frequency generation (SFG) [2–7] have been demonstrated. Realization of low-power, high-efficiency frequency conversion devices could have important applications in quantum information processing. Target applications include on-chip frequency down-conversion of flying qubits, emitted by solid-state emitters such as InAs quantum dots (QDs) or impurities in diamond to telecommunications wavelengths [8] or up-conversion to the optimal frequency window for single-photon detection [9]. Additional applications include on-chip low-power spectroscopic sources, up-conversion of mid-IR to visible for imaging applications [10], and fundamental science studies such as strong coupling of single photons [11] or single-photon blockade [12]. However, for $\chi^{(2)}$ three-wave mixing processes, which have relatively higher nonlinearities at lower powers, the ability to increase the efficiency at low power levels has been limited by the difficulty in engineering the large frequency separations between modes required for these processes.

One particularly promising candidate for achieving efficient nonlinear frequency conversion is the 1D planar nanobeam photonic crystal cavity [13], with Q factors of $>10^9$ simulated, and Q factors as high as 7.5×10^5 demonstrated [13]. Nanobeam designs for four-wave mixing have been proposed [14] and demonstrated [15], and there have been additional proposals for terahertz frequency generation [16] and broadband frequency conversion of single photons [8] using transverse electric/transverse magnetic polarized nanobeam cavities. Such nanobeam cavities have been fabricated in silicon [17], but have yet to be implemented in high $\chi^{(2)}$ materials. Crossed-nanobeam cavities [18] offer another method for increasing the frequency separation of the modes involved in conversion, as the ability to individually select the wavelength of the two resonances is significantly improved and the thickness of the wafer is less critical; however, such cavities suffer significantly reduced Q factors as the frequency separation between modes is increased.

Here we demonstrate that the combination of lower- and higher-order modes in nanobeam cavities can be used for nonlinear frequency conversion. We characterize nanobeam cavities fabricated in $(111)B = (\bar{1}\,\bar{1}\,\bar{1})$ oriented GaAs membranes via fiber-taper and cross-polarized reflectivity. Finally, we demonstrate SFG with two resonances separated by 700 nm. We note that the use of (111) GaAs (as opposed to (001) GaAs) is necessary to enable conversion between three resonances (two for SHG), as discussed in our earlier work [7].

We first consider the band diagram of a nanobeam with lattice constant a, beam width $w = 1.2a$, hole height $h_y = 0.7w$, hole width $h_x = 0.5a$, thickness $t/a = 0.4$, and refractive index of 3.34 (GaAs at 1.8 μm) simulated with MIT photonic bands (MPB) [19], as shown in Fig. 1(a). Due to mirror symmetry in the xy plane of the nanobeam, bands can be described as having either transverse electric-like (TE) polarization, such that $H_x = H_y = E_z = 0$ in the central xy plane, or transverse magnetic-like (TM) polarization, such that $E_x = E_y = H_z = 0$ in the central xy plane [20]. TE bands are indicated by solid blue lines and TM bands by green dashed lines, and the light line indicated by the red line in Fig. 1(b). A gentle perturbation in the periodic structure can localize one of these bands to the perturbed region, generating high-quality factor (Q) and low mode volume (V) confined modes, which we can use to resonantly enhance nonlinear frequency conversion processes. For this experiment, we choose to confine modes from the TE_{000} and TE_{110} bands, as these have an appropriate symmetry and frequency separation. The i, j, k subscripts refer to the number of nodes in the H_z field component in the x, y, and z directions. The confinement is done using a lithographically defined linear tapering of h_x, h_y, and a, with each reduced to a minimum of 0.8 of the value in the untapered region. The first five modes confined from the

 © 2014 Optical Society of America

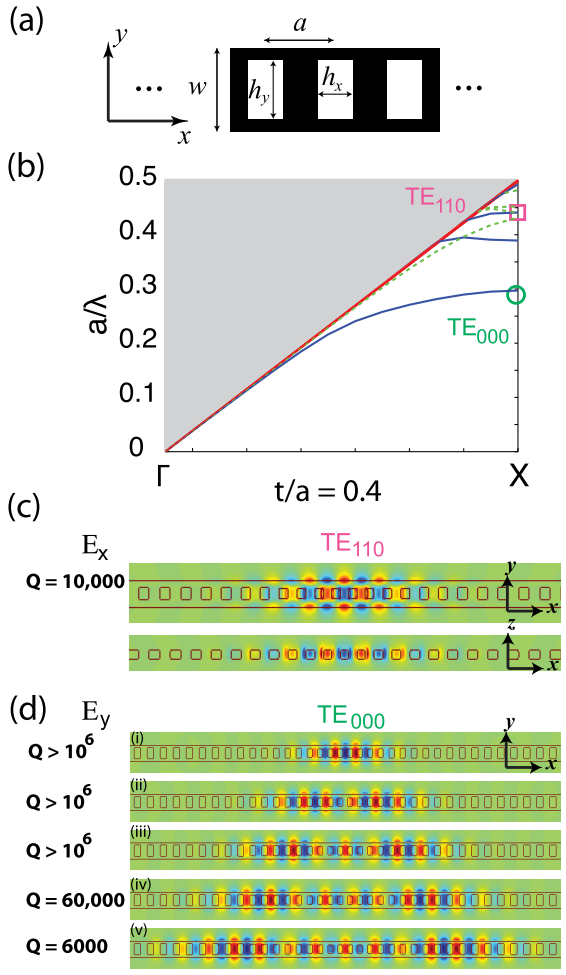

Fig. 1. (a) Illustration of the periodic nanobeam. (b) Band diagram for nanobeam with $h_y = 0.7w$, $h_x = 0.5a$, and $n = 3.34$ for membrane thickness $t = 0.4a$. The blue solid lines show TE modes and the green dashed lines show TM modes. (c) The E_x field component of the localized TE_{110} mode used in this experiment. (d) The E_y field component of the first- to fifth-order TE modes localized by the presence of the cavity from the TE_{000} band in order of increasing frequency.

TE_{000} band for a membrane thickness of $t/a = 0.4$, beam width $w/a = 1.2$, $h_y = 0.7w$, and $h_x = 0.5a$ are shown in Fig. 1(d). We simulated cavity modes using a custom FDTD code developed in our group to run on GPU processors. The modes alternate even and odd with respect to $x = 0$ and have a decreasing Q factor and increasing extent (mode volume) with decreasing frequency. The mode volumes are $0.6(\lambda/n)^3$, $1.1(\lambda/n)^3$, $1.3(\lambda/n)^3$, $1.6(\lambda/n)^3$, and $1.9(\lambda/n)^3$. Similarly, for the TE_{110} band, several modes can be localized, and we obtain a Q factor of 10,000, which can be further optimized with the membrane thickness and hole-size parameters [21]. We note that this is not the only higher-order mode of the nanobeam that is localized with high Q; the other modes in Fig. 1(b) can also be localized with high Q by optimization of various parameters, and these modes may also be used for other nonlinear frequency conversion processes, as will be discussed in more detail in [21].

We fabricate nanobeams in a 250 nm membrane in (111)B oriented GaAs with lattice constants a from 450 to 650 nm (corresponding to $t/a = 0.56$–0.38) and beam widths from 1.07 to 1.5 a as described previously [5]. The nanobeam is fabricated with the x axis (as defined in [Fig. 1(a)]) along the $[0\bar{1}1]$ direction. The rest of the design follows the previous description. The highest frequency localized resonances of the TE_{000} band of the nanobeam (which we will call the fundamental resonance) span from 1.45 to 1.87 μm with lattice-constant variation, with the longest wavelength mode (the fifth confined mode of the band) measured at 2.03 μm. Resonances up to 1.65 μm could be characterized via cross-polarized reflectivity [5]. However, longer wavelength modes were characterized via fiber-taper probing [22], as the cross-polarized reflectivity method did not have high enough signal to noise. In each case the cavity was probed with a broadband tungsten halogen white-light source and reflected/transmitted signal detected on an extended InGaAs spectrometer. An example of such a fiber-taper measurement for a cavity, showing the first five confined TE_{000} modes is shown in Fig. 2(a) for a structure with lattice constant 620 nm ($t/a = 0.4$). The Q factors for the modes are all 8000–10,000, and measurements at shorter wavelengths via both cross-polarized reflectivity and fiber taper indicate these Q factors are limited by coupling to the fiber taper.

We also characterized the higher-order modes of the structure. For the structure characterized in Fig. 2(a), we observed two closely spaced higher-order modes with Q of around 3000 via cross-polarized reflectivity (Fig. 2(b)). We note that the smaller peaks observed in Fig. 2(b) part (i) are from the Fabry–Perot effects due to the optics used and are insignificant. Since the membrane thickness $t/a \approx 0.4$, we believe these modes to be the first two confined (even and odd) TE_{110} modes of the structure. The simulated even mode is shown in Fig. 1(c), with a simulated Q factor of 10,000. The highest Q higher-order modes that we have measured have Q factors of around 8000 at 1300 nm.

We next demonstrate SFG in a nanobeam cavity utilizing a confined TE_{000} mode and TE_{110} mode of the nanobeam. A tunable CW optical parametric oscillator (OPO) is matched to the wavelength of the fourth confined TE_{000} mode of the nanobeam shown in Fig. 2(a) at

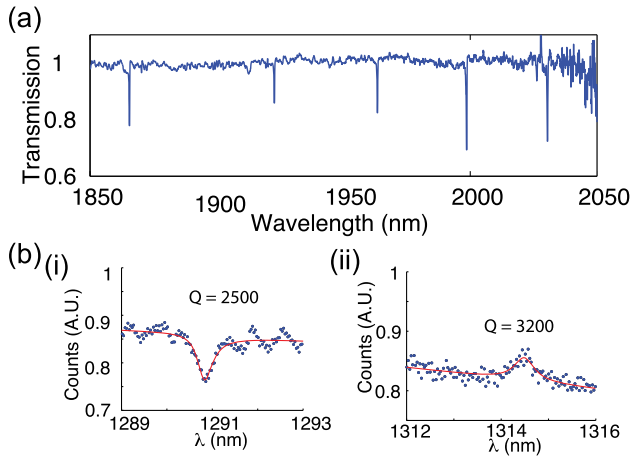

Fig. 2. (a) Linear characterization of a nanobeam at longer wavelengths using the fiber-taper method. (b) Cross-polarized reflectivity measurement (free space) of the TE_{110} modes of the nanobeam cavity in part (a).

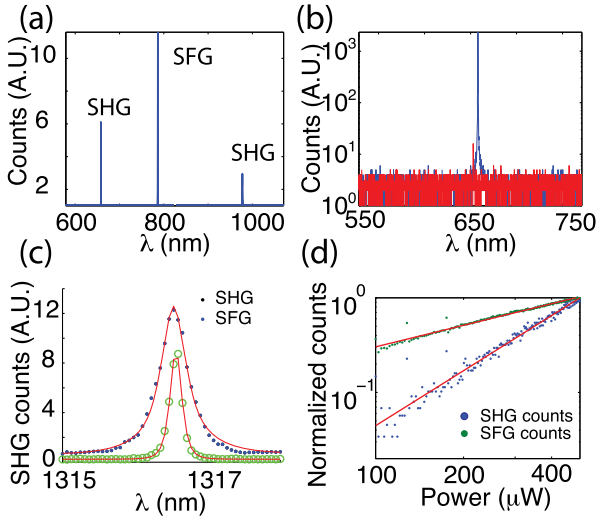

Fig. 3. (a) SHG from the two modes (at 1314.5 and 1955 nm, respectively), as well as SFG. (b) SHG with the tunable diode laser on resonance with the cavity (blue) and off resonance with the cavity (red). (c) Plot of SH and SF versus laser wavelength. The fit is to a Lorentzian squared for SHG and Lorentzian for SFG. (d) As the power of the laser is scanned, the SH follows a quadratic relation, while the SFG follows a sublinear relation.

1955 nm, and is coupled to the mode at normal incidence through a high numerical aperture (NA = 0.95) objective lens (see [7] for details of the experimental setup). A Santec tunable diode laser is similarly matched to the higher-order mode of the nanobeam at 1314.5 nm. SHG and SFG from the two modes are collected back through the same objective lens when the laser is resonant with that mode. The SHG/SFG signal could either be sent to an imaging camera where either real space or momentum space was imaged, or to a spectrometer for spectral resolution. The SH and SF peaks are shown in Fig. 3(a). The tunable diode laser is scanned across the mode in order to verify that the mode is resonantly enhancing the SH efficiency. SHG can still be detected when the laser is far off resonance with the resonant frequency of the cavity; in addition, while the laser must be focused on the nanobeam for this to be observed, it is not necessary for the laser to be focused on the central cavity region. However, there is a 200-fold enhancement in the signal when it is resonant with the mode of the cavity, as shown in Fig. 3(b). This is perhaps due to enhanced in- and out-coupling or surface SHG [23,24] at the many additional etched surfaces of the GaAs. The tunable diode laser was scanned across the higher-order mode at 1314.5 nm, and the SHG and SFG power was monitored versus this laser wavelength. As shown in Fig. 3(c) the SH counts are fit to a Lorentzian squared, while the SF counts are fit to a Lorentzian, both indicating Q factors of between 3000 and 4000, which is also consistent with the cross-polarized reflectivity measurement on this structure. We scan the power of the tunable diode laser, while on resonance with the higher-order mode, from 100 to 400 μW. The OPO power is kept at 500 μW for the SFG scan. On a log–log plot, we obtain a straight line for the SH counts, with a slope of 1.93, which is close to the expected value of 2. The SF is expected to be a straight line with a slope of 1; however, we find that it is nonlinear

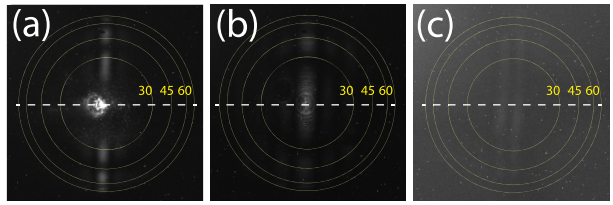

Fig. 4. (a) k-space image of the SH of the 1300 nm coupled laser. (b) k-space image of the SH from the 1955 nm laser. (c) k-space image of the sum frequency. The orientation of the nanobeam is indicated by the dashed white line. The yellow rings indicate light emitted at 30°, 45°, and 60°, with the outer ring corresponding to 71.8°, corresponding to the NA = 0.95 of our objective lens.

on both a log–log plot and a linear plot, and the best fit is for an exponent of 0.75. This indicates nonlinear dependence on the laser power, which could be due to absorption or the laser power being diverted to SHG. The higher-order mode is above twice the bandgap of GaAs, allowing significant two-photon absorption, while both the SHG and SFG are above the bandgap of the GaAs.

We also measure the experimental momentum space (k-space) distribution of the SH and SF from both cavity modes, which shows us the angular distribution of the emitted SH and SF light. This is shown in Fig. 4, with the position of the nanobeam indicated by the dashed white line. The k-space distribution can be used to help identify the low-Q higher-order modes that are taking part in the process. The overlap of the confined TE_{000} and TE_{110} modes with this mode in part determines the efficiency of the process [7], and will be discussed in more detail in [21]. At low powers, the efficiency of SHG and SFG will be proportional to $\eta_1\ \eta_2\ Q_1\ Q_2$, where η_i is the coupling efficiency at ω_i. Since in our experimental setup we couple at normal incidence, η and Q are related, and therefore increasing the Q will not necessarily increase the conversion efficiency. Therefore, in order to achieve efficient frequency conversion, it is also important to engineer input and output coupling ports. For nanobeam photonic crystal cavities, this can be done via a side-coupled waveguide [25].

We have demonstrated the design, fabrication, and characterization of nanobeam cavities with multiple higher-order modes with frequency separations of greater than 700 nm and spanning the range of 1300–2000 nm. We use SFG with light input on these modes to upconvert light from 1300 to 780 nm with the signal at 1955 nm, and also demonstrate SHG from these long wavelength resonances to near infrared wavelengths. The design presented in this Letter could prove useful for frequency conversion between emitters (e.g., Si vacancy in diamond) and telecommunications wavelengths. Our design can also be easily optimized for conversion between other wavelengths, such as 930 nm (InAs QD emission) and 1550 nm (optimal telecommunication-transmission window). Future work could use inverse design [26] or genetic algorithms [27] to optimize resonances at widely spaced frequencies.

Financial support provided by the Air Force Office of Scienepsic Research, MURI Center for multifunctional light–matter interfaces based on atoms and solids,

National Science Graduate Fellowships, and Stanford Graduate Fellowships. This work was performed in part at the Stanford Nanofabrication Facility of NNIN supported by the National Science Foundation under Grant No. ECS-9731293, and at the Stanford Nano Center. J. V. thanks the Alexander von Humboldt Foundation for support.

References

1. Y. Takahashi, Y. Inui, M. Chihara, T. Asano, R. Terawaki, and S. Noda, Nature **498**, 470 (2013).
2. M. Galli, D. Gerace, K. Welna, T. F. Krauss, L. O'Faolain, G. Guizzetti, and L. C. Andreani, Opt. Express **18**, 26613 (2010).
3. M. W. McCutcheon, J. F. Young, G. W. Rieger, D. Dalacu, S. Frédérick, P. J. Poole, and R. L. Williams, Phys. Rev. B **76**, 245104 (2007).
4. K. Rivoire, Z. Lin, F. Hatami, W. T. Masselink, and J. Vučković, Opt. Express **17**, 22609 (2009).
5. S. Buckley, M. Radulaski, K. Biermann, and J. Vučković, Appl. Phys. Lett. **103**, 211117 (2013).
6. Y. Ota, K. Watanabe, S. Iwamoto, and Y. Arakawa, Opt. Express **21**, 19778 (2013).
7. S. Buckley, M. Radulaski, J. Petykiewicz, K. G. Lagoudakis, J.-H. Kang, M. Brongersma, K. Biermann, and J. Vučković, ACS Photon. **1**, 516 (2014).
8. M. W. McCutcheon, D. E. Chang, Y. Zhang, M. D. Lukin, and M. Lončar, Opt. Express **17**, 22689 (2009).
9. C. Langrock, E. Diamanti, R. V. Roussev, Y. Yamamoto, M. M. Fejer, and H. Takesue, Opt. Lett. **30**, 1725 (2005).
10. Q. Zhou, K. Huang, H. Pan, E. Wu, and H. Zeng, Appl. Phys. Lett. **102**, 241110 (2013).
11. W. T. M. Irvine, K. Hennessy, and D. Bouwmeester, Opt. Lett. **96**, 057405 (2006).
12. A. Majumdar and D. Gerace, Phys. Rev. B **87**, 235319 (2013).
13. P. B. Deotare, M. W. McCutcheon, I. W. Frank, M. Khan, and M. Lončar, Appl. Phys. Lett. **94**, 121106 (2009).
14. Z. Lin, T. Alcorn, M. Lončar, S. G. Johnson, and A. W. Rodriguez, "High-efficiency degenerate four wave-mixing in triply resonant nanobeam cavities," arXiv:1311.4100 (2013).
15. S. Azzini, D. Grassani, M. Galli, D. Gerace, M. Patrini, M. Liscidini, P. Velha, and D. Bajoni, Appl. Phys. Lett. **103**, 031117 (2013).
16. I. B. Burgess, Y. Zhang, M. W. McCutcheon, A. W. Rodriguez, J. Bravo-Abad, S. G. Johnson, and M. Lončar, Opt. Express **17**, 20099 (2009).
17. M. W. McCutcheon, P. B. Deotare, Y. Zhang, and M. Lončar, Appl. Phys. Lett. **98**, 111117 (2011).
18. K. Rivoire, S. Buckley, and J. Vučković, Appl. Phys. Lett. **99**, 013114 (2011).
19. S. Johnson and J. Joannopoulos, Opt. Express **8**, 173 (2001).
20. J. D. Joannopoulos, S. G. Johnson, J. N. Winn, and R. D. Meade, *Photonic Crystals: Molding the Flow of Light*, 2nd ed. (Princeton University, 2011).
21. S. Buckley, M. Radulaski, J. L. Zhang, J. Petykiewicz, K. Biermann, and J. Vučković, "Multimode nanobeam cavities for nonlinear optics: high quality resonances separated by an octave," arXiv:1408.6567 (2014).
22. G. Shambat, Y. Gong, J. Lu, S. Yerci, R. Li, L. Dal Negro, and J. Vučković, Opt. Express **18**, 5964 (2010).
23. R. Sanatinia, M. Swillo, and S. Anand, Nano Lett. **12**, 820 (2012).
24. M. W. McCutcheon, G. W. Rieger, I. W. Cheung, J. F. Young, D. Dalacu, S. Frédérick, P. J. Poole, G. C. Aers, and R. L. Williams, Appl. Phys. Lett. **87**, 221110 (2005).
25. S. Gröblacher, J. T. Hill, A. H. Safavi-Naeini, J. Chan, and O. Painter, Appl. Phys. Lett. **103**, 181104 (2013).
26. J. Lu and J. Vučković, Opt. Express **21**, 13351 (2013).
27. M. Minkov and V. Savona, Proc. SPIE **9127**, 91270C (2014).